

Finite elements for the space approximation of a differential model for salts crystallization

*^oA. Aimi , ^{†o}G. Bretti , ^{*o}G. Di Credico , [§]F. Freddi ,
^{*o}C. Guardasoni  and ^{‡◊o}M. Pezzella 

*Dept. of Mathematical Physical and Computer Sciences, University of Parma, Italy

^oMembers of the INdAM-GNCS Research Group, Italy

[†]National Research Council of Italy, Institute for Applied Mathematics “M. Picone”, Rome branch, Italy

[§]Department of Engineering and Architecture, University of Parma, Italy

[‡]National Research Council of Italy, Institute for Applied Mathematics “M. Picone”, Naples branch, Italy

[◊]Dept. of Mathematics and Applications R. Caccioppoli, University of Naples Federico II, Italy

Abstract

This article investigates a space-time differential model related to the degradation of stone artifacts caused by exposure to air and atmospheric agents, which specifically lead to the accumulation of salt crystals in the material. A numerical method based on finite-element space discretization and implicit-explicit time marching is proposed as an extension of the one-dimensional finite-difference framework introduced in [5]. Within the same one-dimensional setting, a sensitivity analysis is performed, based on the techniques developed therein. They are also used as a comparison tool for the finite-element formulation, here introduced for more realistic simulations in higher space dimensions. Considerations about stability will be provided, together with an experimental convergence analysis highlighting the performance of the proposed approach. Numerical results in two and three space dimensions, obtained by an efficient code implementation, will be presented and discussed.

KEYWORDS: Finite element method - Finite difference method - Mathematical model - Salt crystallization - Porous media

MATHEMATICS SUBJECT CLASSIFICATION (MSC 2020): 65M60 - 65M06 - 65Z05 - 76S05 - 93B35

1 Introduction

Lapideous materials used in cultural heritage can be regarded as porous media, permeable to damaging agents transported by moisture which may lead to structural deterioration. When exposed to environmental factors, stones undergo weathering processes driven by water penetration, whether from meteoric precipitation or groundwater infiltration. Numerous studies have investigated the degradation of porous building materials in heritage structures (see, for instance, [10, 12] and references therein). Degradation of monumental stones arises from a combination of physical-mechanical, chemical and biological processes. Physical-mechanical effects include salt crystallization [14], erosion [20] and thermal expansion [29]. Chemical reactions, such as carbonation [8, 16], sulfation [2, 4], oxidation [28] and hydration [15, 30], alter the material composition, producing clay, crusts that swell, soluble salts and shrinkage. In addition, the growth of biological entities, including plants [31], mosses, lichens and bacte-

ria [32], contributes to further deterioration. The interplay of these effects may induce microstructural changes in the material, sustaining an ongoing decay.

In this work, we focus on salt crystallization processes, which constitute one of the main causes of deterioration in porous materials. The phenomenon involves capillary penetration and internal reactions of salts dissolved in water flowing through the stone pores. Under certain conditions, the salts precipitate, forming crystals either on the surface (efflorescence) or within the pores (subflorescence). When crystallization occurs within the pores, it reduces the available pore volume, disrupts the liquid network and slows water transport, with consequent effects on the material deterioration.

In a context where preventive strategies play a critical role, several differential models have been proposed to characterize and quantify the degradation, alongside numerical methods specifically developed for its simulation. These models account for water transport in the porous medium, incorporating Darcys law, the changes in porosity due to crystal blooming and the effects of protective treatments aimed at mitigating the damage [5, 9]. Existence and uniqueness results for the model in [5], both without and with boundary conditions, are provided in [17, 18]. However, despite their modeling potential, the existing mathematical frameworks are based on a one-dimensional spatial representation. Although capable of describing vertical rise in porous materials, these models find limited applicability in realistic case studies. The first contribution of this work consists in the extension the model of [5] to multidimensional domains, that provides a more detailed investigation of diffusion-driven phenomena. Furthermore, to address the challenges inherent in multidimensional simulations, a Finite Element Method (FEM) approach is employed. FEM provides a flexible and robust framework for the discretization of complex geometries and heterogeneous domains, ensuring accurate representation of the underlying physics. A comparison between FEM and traditional one-dimensional finite difference (FD) schemes, together with a discussion of their respective advantages and limitations, is reported in [34].

1.1 General description of the model problem

In this paper, we build upon the mathematical model introduced in [5], describing the coupled processes of moisture transport, salt migration and crystallization in porous materials exposed to saline water and atmospheric agents. The formulation is motivated by standard laboratory imbibition-drying experiments performed on stone- and brick-like specimens, where salt accumulation within the pore network leads to progressive porosity reduction and material degradation.

The physical domain here considered is a bounded region $\Omega \subset \mathbb{R}^d$, with $d = 1, 2, 3$, representing a prismatic porous specimen subjected to water absorption from the bottom surface and moisture exchange with the surrounding air at the exposed boundaries. The evolution of the system is studied over a finite time interval $[0, T]$, which may be decomposed into an imbibition phase followed by a drying phase in order to reproduce the experimental protocol.

The model accounts for the interaction between a liquid phase carrying dissolved salt ions and a solid crystalline phase precipitating within the pore space. A key feature of the formulation is the explicit coupling between transport processes and microstructural evolution induced by salt crystallization.

1.2 State variables

The unknowns of the problem are four space- and time-dependent fields defined for $(\mathbf{x}, t) \in \Omega \times [0, T]$:

- $\theta_l(\mathbf{x}, t)$, the volumetric fraction of liquid water, representing the portion of the pore volume locally occupied by the liquid phase;
- $c_i(\mathbf{x}, t)$, the concentration of dissolved salt ions transported by the liquid phase;
- $c_s(\mathbf{x}, t)$, the concentration of crystallized salt deposited within the pore network;

- $n(\mathbf{x}, t)$, the porosity of the material, defined as the fraction of the total volume available for fluid transport.

The porosity n is not treated as an independent field, but is coupled to the crystallized salt concentration through a constitutive relation accounting for pore clogging due to crystal growth. As crystallization progresses, the available pore volume is reduced, which in turn affects the transport properties of the medium.

1.3 Governing mechanisms

Moisture transport is described by a nonlinear diffusion process driven by capillary effects and modulated by the evolving porosity. The effective permeability of the medium depends on the saturation ratio θ_l/n through a nonlinear function calibrated to reproduce experimentally observed absorption behavior in porous materials. This formulation allows the model to capture saturation-dependent mobility and sharp wetting fronts.

The transport of dissolved salt ions is governed by a convection–diffusion mechanism. Advection is induced by the moisture flux, while molecular diffusion accounts for concentration gradients within the liquid phase. The ion balance is coupled to the crystallization kinetics, which acts as a sink term for the dissolved salt and a source term for the solid phase.

Salt crystallization is modeled through a kinetic law depending on the local ion concentration and the available pore space. The precipitation of crystals reduces the porosity, which feeds back into the moisture and ion transport equations, resulting in a strongly coupled nonlinear system.

1.4 Experimental setting and scope

Boundary conditions are chosen to reproduce standard imbibition–drying experiments. During the imbibition phase, the bottom boundary of the specimen is assumed to be in contact with a saline solution, prescribing saturated moisture and ion concentration. At the exposed boundaries, moisture exchange with the external environment is modeled through Robin-type conditions, while no-flux (homogeneous Neumann) conditions are imposed for the salt ions. During the drying phase the boundary conditions are modified to simulate evaporation and the absence of further salt supply.

The resulting model consists of a system of nonlinear, time-dependent partial differential equations with strong coupling between transport, reaction, and microstructural evolution. The formulation is posed in a general spatial dimension d , enabling one-dimensional simulations for calibration and sensitivity analysis, as well as higher-dimensional computations for more realistic geometries.

The aim of the model is to provide a predictive and numerically tractable framework for the analysis of salt-induced degradation phenomena in porous materials, with particular emphasis on the interplay between moisture dynamics, crystallization processes, and porosity variation.

The original contribution of the present work is therefore given by the following aspects: i) a multi-dimensional extension of the 1D model in [5] is provided; ii) a sensitivity analysis on model parameters is carried out in the 1D formulation; iii) a stable and convergent FEM based solver is developed and implemented to simulate 2D and 3D geometries.

The paper is organized as follows: Section 2 describes in detail the differential problem with its initial and boundary conditions, for both the imbibition and the drying phases; sensitivity analysis is developed in Section 3, while the description of the space-time discretization is written in Section 4. Numerical results are presented and discussed in Section 5, together with an experimental convergence analysis, while conclusions are collected in Section 6. For the interested reader, the description of the calibration of the top-boundary exchange coefficient can be found in Appendix A, while, to make the paper self-contained, the original 1D space-time finite differences scheme is briefly reported in Appendix B.

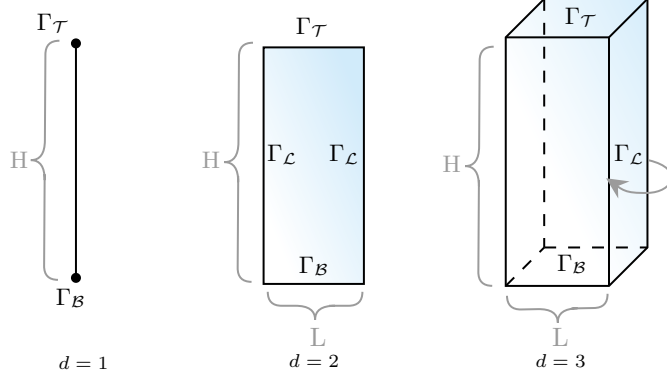


Figure 1: Geometrical representation of the domain Ω for $d = 1, 2, 3$, together with a schematic representation of the partition set on the boundary Γ .

2 The differential problem

For the sake of simplicity, the space domain of the model problem will be represented by a d -dimensional prism

$$\Omega = \{\mathbf{x} \in \mathbb{R}^d \mid (x_1, \dots, x_{d-1}) \in [-L/2, L/2]^{d-1}, x_3 \in [0, H]\},$$

being $L > 0$ and $H > 0$ its height. We adopt the convention that, if $d = 1$, the physical domain reduces to the line interval $\Omega = [0, H]$ and the 1D space variable can be written equivalently as x_3 or x . The boundary $\partial\Omega = \Gamma$ is partitioned as the union of the sets Γ_τ , Γ_B and Γ_L , where

$$\Gamma_\tau = \{\mathbf{x} \in \Omega \mid x_3 = H\}, \quad \Gamma_B = \{\mathbf{x} \in \Omega \mid x_3 = 0\},$$

are respectively the top base and the bottom base of the prism (reducing just to the two extremes of the interval $[0, H]$ for the 1D case), while the lateral edges of the prism are defined by $\Gamma_L = \Gamma \setminus (\Gamma_B \cup \Gamma_\tau)$, see Figure 1.

2.1 Water absorption phase

In this phase of the experiment, considered in the time domain $[0, T]$, the lower base Γ_B is supposed to be in contact with a salty water solution, seeping vertically along the height of the prism and depositing salt crystals in its volume. At the top base Γ_τ , interactions with the external environment are allowed, especially the drying action of the air. Imbibition from the bottom base induces the following sets of initial conditions, given for all dimensions $d = 1, 2, 3$:

$$\begin{aligned} \theta_l(\mathbf{x}, 0) &= \begin{cases} n_0 & \text{for } \mathbf{x} \in \Gamma_B \\ \bar{\theta}_l & \text{for } \mathbf{x} \in \Omega \setminus \Gamma_B \end{cases}, & c_i(\mathbf{x}, 0) &= \begin{cases} \bar{c}_i & \text{for } \mathbf{x} \in \Gamma_B \\ 0 & \text{for } \mathbf{x} \in \Omega \setminus \Gamma_B \end{cases}, \\ c_s(\mathbf{x}, 0) &= 0 \quad \text{for } \mathbf{x} \in \Omega, & n(\mathbf{x}, 0) &= n_0 \quad \text{for } \mathbf{x} \in \Omega, \end{aligned} \quad (1)$$

and the following Dirichlet constraints for θ_l and c_i on $\Gamma_B \times [0, T]$:

$$\begin{cases} \theta_l(\mathbf{x}, t) = n_0 & \text{for } (\mathbf{x}, t) \in \Gamma_B \times [0, T] \\ c_i(\mathbf{x}, t) = \bar{c}_i & \text{for } (\mathbf{x}, t) \in \Gamma_B \times [0, T] \end{cases}. \quad (2)$$

The positive parameters n_0 and $\bar{\theta}_l$ in (1) indicate, respectively, the porosity of the material and the moisture content in ambient air, while \bar{c}_i is the sodium sulfate concentration in water.

Interaction with the air at the top of the brick is included by imposing Robin and Neumann conditions, respectively, for θ_l and c_i :

$$\begin{cases} \nabla \theta_l(\mathbf{x}, t) \cdot \mathbf{n} = K_w (\bar{\theta}_l - \theta_l(\mathbf{x}, t)) & \text{for } (\mathbf{x}, t) \in \Gamma_T \times [0, T] \\ \nabla c_i(\mathbf{x}, t) \cdot \mathbf{n} = 0 & \text{for } (\mathbf{x}, t) \in \Gamma_T \times [0, T] \end{cases}, \quad (3)$$

being $\mathbf{n} := \mathbf{n}(\mathbf{x}) \in \mathbb{R}^d$ the normal outward pointing vector at the point $\mathbf{x} \in \Gamma$. The loss of humidity at the top of the brick is addressed by the Robin constraint imposed on θ_l over $\Gamma_T \times [0, T]$, with the positive constant K_w controlling the intensity of the exchange with the external environment. This boundary treatment differs from that adopted in [5], where moisture exchange is described through an implicit nonlinear relation. Although physically detailed, that formulation is computationally demanding and does not naturally extend to multidimensional settings. Conversely, the choice in (3) ensures well-posedness and straightforward applicability in higher dimensions. Consistency with the original model is retained by calibrating K_w to reproduce, in the one-dimensional case, the same global dynamical behavior observed in [5] for the two-phase imbibition drying experiment. Details are provided in Appendix A.

Exclusively for $d > 1$, the presence of the lateral sides Γ_L compels the definition of null flux constraints for quantities θ_l and c_i :

$$\begin{cases} \nabla \theta_l(\mathbf{x}, t) \cdot \mathbf{n} = 0 & \text{for } (\mathbf{x}, t) \in \Gamma_L \times [0, T] \\ \nabla c_i(\mathbf{x}, t) \cdot \mathbf{n} = 0 & \text{for } (\mathbf{x}, t) \in \Gamma_L \times [0, T] \end{cases}, \quad (4)$$

simulating the isolation of this portion of the boundary from the external environment, a condition obtainable in laboratory covering the porous prism by a layer of tape. Figure 2 (left) provides a schematic three-dimensional representation of the imbibition phase.

2.2 Drying phase

The final quantities $\theta_l^T(\mathbf{x}) := \theta_l(\mathbf{x}, T)$, $c_i^T(\mathbf{x}) := c_i(\mathbf{x}, T)$, $c_s^T(\mathbf{x}) := c_s(\mathbf{x}, T)$ and $n^T(\mathbf{x}) := n(\mathbf{x}, T)$ obtained by the previous phase are used as initial conditions for the subsequent drying phase, whose time domain will be denoted by $[0, \tilde{T}]$. In fact, to be significant from the experimental point of view, this requires to investigate the dynamics starting from the spatial domain Ω saturated by humidity:

$$\theta_l(\mathbf{x}, 0) = \theta_l^T(\mathbf{x}), \quad c_i(\mathbf{x}, 0) = c_i^T(\mathbf{x}), \quad c_s(\mathbf{x}, 0) = c_s^T(\mathbf{x}), \quad n(\mathbf{x}, 0) = n^T(\mathbf{x}) \quad \text{for } \mathbf{x} \in \Omega. \quad (5)$$

The simulation of the drying test requires a modification of the boundary conditions. In fact, we prescribe null flux for c_i on the entire boundary, namely

$$\nabla c_i(\mathbf{x}, t) \cdot \mathbf{n} = 0 \quad \text{for } (\mathbf{x}, t) \in \Gamma \times [0, \tilde{T}]. \quad (6)$$

For θ_l at the boundary, we prescribe

$$\begin{cases} \theta_l(\mathbf{x}, t) = 0 & \text{for } (\mathbf{x}, t) \in \Gamma_B \cup \Gamma_T \times [0, \tilde{T}] \\ \nabla \theta_l(\mathbf{x}, t) \cdot \mathbf{n} = 0 & \text{for } (\mathbf{x}, t) \in \Gamma_L \times [0, \tilde{T}] \end{cases}. \quad (7)$$

The Dirichlet constraints in (7) for θ at the top and bottom of the brick simulate the absence of humidity on the surface required to dry the brick. We refer to Figure 2 (right) for a schematic three-dimensional representation of the drying phase.

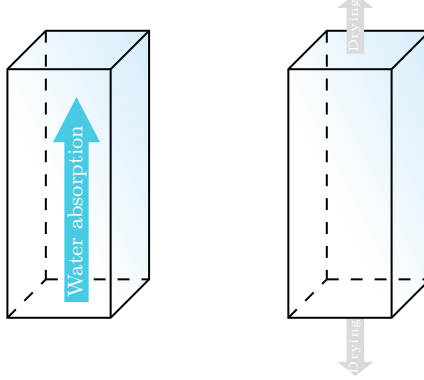


Figure 2: Schematic geometrical representation of the imbibition (left) and drying (right) phases.

2.3 The governing equations

The growth of salt particles in Ω , both in water absorption and in drying dynamics, is defined by the following system of equations, taken from [5]:

$$\frac{\partial \theta_l}{\partial t}(\mathbf{x}, t) = \operatorname{div} \left(\left(\frac{n(\mathbf{x}, t)}{n_0} \right)^2 \nabla B \left(\frac{\theta_l(\mathbf{x}, t)}{n(\mathbf{x}, t)} \right) \right), \quad (8)$$

$$\frac{\partial c_s}{\partial t}(\mathbf{x}, t) = K_s c_i(\mathbf{x}, t) (n(\mathbf{x}, t) - \theta_l(\mathbf{x}, t))^2 + \bar{K} (c_i(\mathbf{x}, t) - \bar{c})_+ \theta_l(\mathbf{x}, t) \quad (9)$$

$$n(\mathbf{x}, t) = n_0 - \gamma c_s(\mathbf{x}, t), \quad (\mathbf{x}, t) \in \Omega \times [0, T], \quad (10)$$

$$\frac{\partial}{\partial t} (\theta_l(\mathbf{x}, t) c_i(\mathbf{x}, t)) = \operatorname{div} \left(c_i(\mathbf{x}, t) \left(\frac{n(\mathbf{x}, t)}{n_0} \right)^2 \nabla B \left(\frac{\theta_l(\mathbf{x}, t)}{n(\mathbf{x}, t)} \right) + D \theta_l(\mathbf{x}, t) \nabla c_i(\mathbf{x}, t) \right) - \frac{\partial c_s}{\partial t}(\mathbf{x}, t), \quad (11)$$

where constants K_s and D are positive rates of crystallization and diffusivity, γ indicates the crystal volume and $(\cdot)_+$ denotes the positive part of a function. The gradient operator $\nabla(\cdot)$ in (8) and (11) performs exclusively spatial derivatives and the function $B(s)$, defined as the following piece-wise third-degree polynomial function

$$B(s) = \begin{cases} 0 & \text{if } s < a, \\ \frac{2}{3}c \left(\left(\frac{1-s}{1-a} \right)^2 (3a-1-2s) + (1-a) \right) & \text{if } s \in [a, 1], \\ \frac{2}{3}c(1-a) & \text{if } s > 1 \end{cases} \quad (12)$$

governs the fluid saturation in the brick. The parameters a and c in (12) are positive constants related to the physical properties of the porous medium. The challenging identification of parameter sets of function $B(\cdot)$ that reproduces the capillary rise properties of specific porous materials is addressed in [6, 7].

Let us finally remark that the equation (8) describing the behavior of θ_l field is a nonlinear PDE. In view of the approximation in space variable using FEM, let us rewrite (8) and (11) in the following compact notation

$$\begin{aligned} \frac{\partial \theta_l}{\partial t} &= \operatorname{div} [f(\theta_l, n) \nabla \theta_l] - \operatorname{div} [F(\theta_l, n) \theta_l] \\ \frac{\partial}{\partial t} (\theta_l c_i) &= \operatorname{div} [c_i (f(\theta_l, n) \nabla \theta_l - F(\theta_l, n) \theta_l)] + D \operatorname{div} [\theta_l \cdot \nabla c_i] - \frac{\partial c_s}{\partial t}, \end{aligned}$$

being $f(\mathbf{x}, t)$ and $F(\mathbf{x}, t)$ the scalar and the vectorial operators

$$f(\theta_l(\mathbf{x}, t), n(\mathbf{x}, t)) = \frac{n(\mathbf{x}, t)}{n_0^2} B' \left(\frac{\theta_l(\mathbf{x}, t)}{n(\mathbf{x}, t)} \right),$$

$$F(\theta_l(\mathbf{x}, t), n(\mathbf{x}, t)) = \frac{1}{n_0^2} B' \left(\frac{\theta_l(\mathbf{x}, t)}{n(\mathbf{x}, t)} \right) \nabla n(\mathbf{x}, t).$$

The exact expression of $B(s)$ derivative is

$$B'(s) = \begin{cases} 0 & \text{if } s < a \vee s > 1, \\ \frac{4c}{(1-a)^2} (1-s)(s-a) & \text{if } s \in [a, 1]. \end{cases} \quad (13)$$

We conclude the Section listing in Table 1 the values of the physical constants, together with their units of measurement, onto which the model problem (1)-(13) depends.

Table 1: Parameters of the imbibition phenomenon simulation as detailed in [13]. The value of K_w is determined as described in Appendix A.

Description	Value	Units
n_0	$2.8510 \cdot 10^{-1}$	—
c	$9.8073 \cdot 10^{-4}$	cm^2/s
a	$2.1904 \cdot 10^{-1}$	—
D	$1.2300 \cdot 10^{-5}$	cm^2/s
$\bar{\theta}_l$	$6.2540 \cdot 10^{-2}$	g/cm^3
\bar{c}_i	$9.9500 \cdot 10^{-2}$	g/cm^3
γ	$6.0000 \cdot 10^{-1}$	cm^3/g
K_s	$4.1000 \cdot 10^{-5}$	s^{-1}
K_w	$1.5 \cdot 10^{-2}$	cm/s
\bar{c}	0.4399	g/cm^3
\bar{K}	$1.0000 \cdot 10^{-4}$	s^{-1}

3 Sensitivity analysis

In order to assess the robustness of the equations (8)–(11) with respect to the parameters that exert the strongest influence on the crystallization dynamics, we carried out a local sensitivity analysis following the approach of [11]. Unlike classical one-at-a-time (OAT) investigations, which vary a single parameter while keeping others fixed, we explore local variations of multiple parameters simultaneously within prescribed bounds. In practice, this corresponds to probing a full neighborhood around the reference parameter set, rather than individual coordinate lines, thus capturing all relevant directional derivatives. In this context, the 1D setting offers a computationally efficient framework. Specifically, we focus on the following three parameters

- γ , the specific volume of the crystals. It determines the amount of pore volume locally occupied by the precipitated solid phase and directly influences the porosity reduction.
- K_s , the crystallization rate. This coefficient governs the speed at which dissolved ions transform into solid crystals and therefore controls the temporal scale of salt accumulation.
- K_w , the exchange coefficient appearing in the Robin-type boundary condition (3) at the top.

The analysis evaluates the effect of perturbations of these parameters on the full evolution of the system, encompassing both the imbibition and drying phases. As sensitivity metrics, we consider the global quantities

$$\mathcal{N}(\gamma, K_s, K_w) = \frac{1}{H} \int_0^H n(x, T_{\text{end}}) dx, \quad \mathcal{C}_s(\gamma, K_s, K_w) = \frac{1}{H} \int_0^H c_s(x, T_{\text{end}}) dx, \quad (14)$$

which represent, respectively, the average porosity and the average amount of crystallized salt at the final time $T_{\text{end}} = T_{\text{imb}} + T_{\text{dry}} = 10$ days + 5 hours. For both metrics, discretized by a fourth order Gregory quadrature rule (see, for instance, [23, 25] and references therein), we evaluate the relative deviation with respect to the baseline parameters (γ^0, K_s^0, K_w^0) . The coefficients $\gamma^0 = 6 \cdot 10^{-1} \text{ cm}^3/\text{g}$ and $K_s^0 = 4.1 \cdot 10^{-5} \text{ s}$ coincide with the ones calibrated in [5] (see Table 1), whereas $K_w^0 = K_w^* = 1.5 \cdot 10^{-2}$ is the optimal value identified with the analysis performed in Appendix A.

To explore the parameter space, we account for increments and decrements of 1% up to a maximum of 10% for each parameter, which yields $21^3 = 9261$ parameter triplets. For each configuration, the complete two-phase simulation is performed up to $T_{\text{end}} = 882000$ s, using the finite difference scheme (25) (see Appendix B) with space and time steps $\Delta x = 0.15 \text{ cm}$ and $\Delta t = 0.25 \text{ s}$. For each run, we compute the relative changes in \mathcal{N} and \mathcal{C}_s with respect to the reference values $\mathcal{N}^0 = \mathcal{N}(\gamma^0, K_s^0, K_w^0)$ and $\mathcal{C}_s^0 = \mathcal{C}_s(\gamma^0, K_s^0, K_w^0)$. Figure 3 reports the results of the local sensitivity analysis, performed as specified

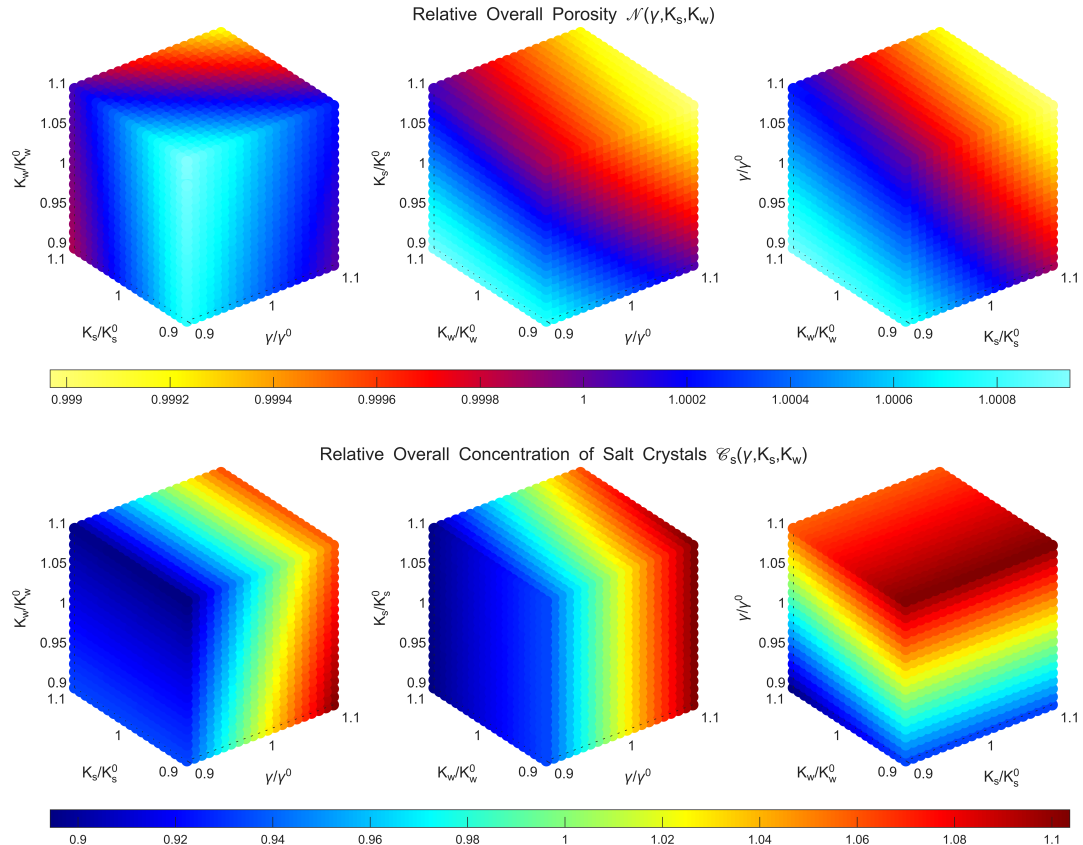


Figure 3: Results of the local sensitivity analysis. Relative changes, with respect to the baseline parameters, in the average porosity (top) and in the average crystallized salt (bottom) at the final time. Each plot illustrates the combined effect of perturbations in γ , K_s , and K_w . (Distinct colormaps and scales are used for the two panels).

above. The model demonstrates strong robustness: even with parameter perturbations up to $\pm 10\%$,

the maximum deviation in \mathcal{N} is 0.94%, while for \mathcal{C}_s it is 10.37%. In both cases, the perturbations do not amplify in the system response. Furthermore, following the one-factor-at-a-time (OAT) approach [27], of which our methodology is an extension, we observe from Figure 4 that the water exchange coefficient K_w has the largest influence on \mathcal{N} , whereas \mathcal{C}_s is more sensitive to variations in the crystallization rate K_s . These results are in full agreement with the physical mechanisms governing the phenomenon.

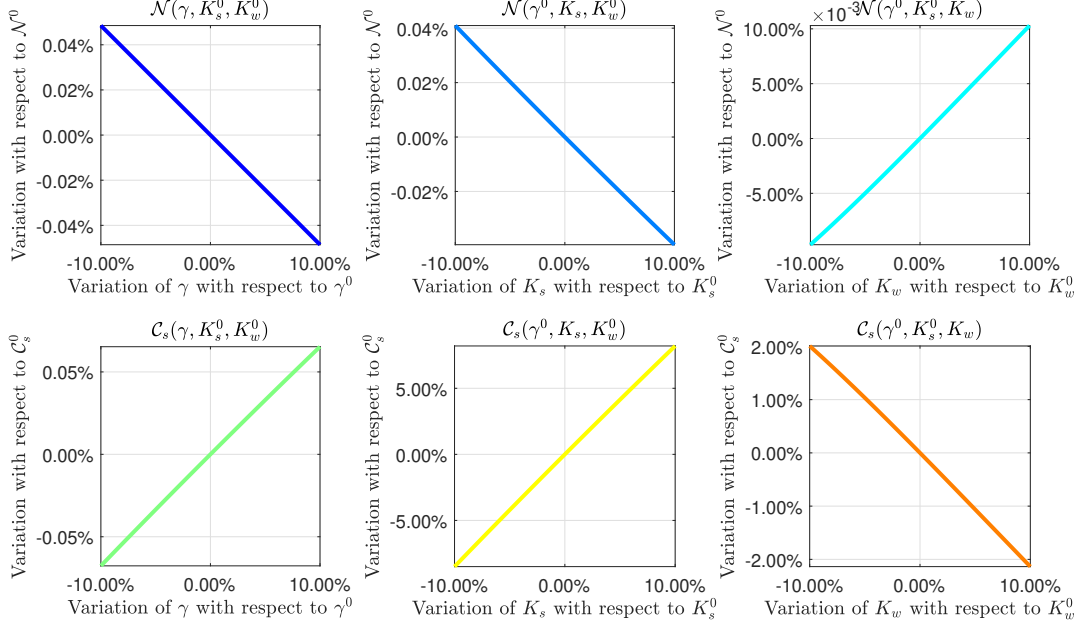


Figure 4: Results of the one-factor-at-a-time (OAT) sensitivity analysis.

Remark 1. In line with the sensitivity analysis discussed above, the calibrated coefficients display stable behavior when applied within the full dynamics. This observation indicates that the parameter values identified in [5], despite being obtained in a different experimental and geometrical configuration, remain suitable for the multidimensional simulations conducted in this work.

4 Finite elements space discretization

In this section we provide a hybrid elaboration of (8)-(11). First of all, we introduce the time discretization: let Δt be the positive time step size and consider the uniform mesh $t_k = k\Delta t$, for $k = 0, \dots, N$, being N such that the final time instant of analysis is given by $N\Delta t$. The four problem unknowns are then approximated by their collocation in time at the generic node t_k :

$$\theta_l^k(\mathbf{x}) \approx \theta_l(\mathbf{x}, t_k), \quad c_s^k(\mathbf{x}) \approx c_s(\mathbf{x}, t_k), \quad c_i^k(\mathbf{x}) \approx c_i(\mathbf{x}, t_k), \quad n^k(\mathbf{x}) \approx n(\mathbf{x}, t_k), \quad k = 0, \dots, N, \quad (15)$$

allowing to approximate the involved time derivatives in terms of finite differences of the first order

$$\frac{\partial \theta_l}{\partial t}(\mathbf{x}, t_{k+1}) \approx \frac{\theta_l^{k+1}(\mathbf{x}) - \theta_l^k(\mathbf{x})}{\Delta t}, \quad \frac{\partial c_s}{\partial t}(\mathbf{x}, t_{k+1}) \approx \frac{c_s^{k+1}(\mathbf{x}) - c_s^k(\mathbf{x})}{\Delta t}, \quad \frac{\partial c_i}{\partial t}(\mathbf{x}, t_{k+1}) \approx \frac{c_i^{k+1}(\mathbf{x}) - c_i^k(\mathbf{x})}{\Delta t}. \quad (16)$$

It is understood that time approximations in (15) are subject to initial conditions (1) for the imbibition phase and to (5) for the drying phase.

The space discretization starts writing the PDEs of the model problem, already discretized in time variable, in weak form. To do this, for the imbibition phase we consider test functions $v_{\theta_l}, v_{c_i} \in$

$H_{\Gamma_B}^1(\Omega) = \{v \in H^1(\Omega) \mid v|_{\Gamma_B} = 0\}$ and we perform the projection of the PDEs (8) and (11) at each time step, obtaining for each $k = 0, \dots, N-1$ the following system of equations in the space unknowns $\theta_l^{k+1}, c_i^{k+1}, c_s^{k+1}$ and n^{k+1} , subjected to (2)-(3):

$$\begin{aligned} \left\langle \frac{\theta_l^{k+1} - \theta_l^k}{\Delta t}, v_{\theta_l} \right\rangle_{\Omega} &= - \left\langle f(\theta_l^k, n^k) \nabla \theta_l^{k+1}, \nabla v_{\theta_l} \right\rangle_{\Omega} + \left\langle f(\theta_l^k, n^k) K_w (\bar{\theta}_l - \theta_l^{k+1}), v_{\theta_l} \right\rangle_{\Gamma_T} \\ &\quad - \left\langle \operatorname{div} [F(\theta_l^k, n^k) \theta_l^{k+1}], v_{\theta_l} \right\rangle_{\Omega}, \end{aligned} \quad (17)$$

$$\frac{c_s^{k+1} - c_s^k}{\Delta t} = K_s c_i^k (n^k - \theta_l^k)^2 + \bar{K} (c_i^k - \bar{c})_+ \theta_l^k, \quad (18)$$

$$n^{k+1} = n_0 - \gamma c_s^{k+1}, \quad (19)$$

$$\begin{aligned} \left\langle \frac{\theta_l^{k+1} c_i^{k+1} - \theta_l^k c_i^k}{\Delta t}, v_{c_i} \right\rangle_{\Omega} &= \left\langle \operatorname{div} \{c_i^{k+1} [f(\theta_l^{k+1}, n^{k+1}) \nabla \theta_l^{k+1} - \theta_l^{k+1} F(\theta_l^{k+1}, n^{k+1})]\}, v_{c_i} \right\rangle_{\Omega} \\ &\quad - \left\langle D \theta_l^{k+1} \nabla c_i^{k+1}, \nabla v_{c_i} \right\rangle_{\Omega} - \left\langle \frac{c_s^{k+1} - c_s^k}{\Delta t}, v_{c_i} \right\rangle_{\Omega}. \end{aligned} \quad (20)$$

The time iterations of the scheme starts from θ_l^0, c_i^0, c_s^0 and n^0 given by the initial conditions (1).

For the drying phase, let us note that $v_{\theta_l} \in H_{\Gamma_B \cup \Gamma_T}^1(\Omega) = \{v \in H^1(\Omega) \mid v|_{\Gamma_B \cup \Gamma_T} = 0\}$ and $v_{c_i} \in H^1(\Omega)$. Moreover, we remark that boundary conditions (7) induce a modification in the weak problem to be solved at each time step: in particular equation (17) simplifies in

$$\left\langle \frac{\theta_l^{k+1} - \theta_l^k}{\Delta t}, v_{\theta_l} \right\rangle_{\Omega} = - \left\langle f(\theta_l^k, n^k) \nabla \theta_l^{k+1}, \nabla v_{\theta_l} \right\rangle_{\Omega} - \left\langle \operatorname{div} [F(\theta_l^k, n^k) \theta_l^{k+1}], v_{\theta_l} \right\rangle_{\Omega}. \quad (21)$$

In this phase, the time iterations start from θ_l^0, c_i^0, c_s^0 and n^0 given by the initial conditions (5).

In the above framework, the space discretization is performed introducing a standard conforming domain mesh, depending on the geometric parameter h , which is defined as the the maximum among triangles or tetrahedrons diameters, respectively, in 2D or 3D (and simplifies as the maximum length of the mesh elements in 1D). Finite dimensional spaces of piece-wise linear finite elements, related to the considered mesh, have been taken into account, to fully approximate the above equations. The hybrid first order FD in time and FEM in space has been set up within FEniCS computing platform [1].

Remark 2. *Let us observe that the weak equation (17) presents an implicit-explicit discretization scheme in time for the θ_l unknown. Moreover, the fully discretized equation coming from (20) does not need the addition of a stabilizing term, as in the fourth equation of the finite differences scheme (25) (see Appendix B).*

5 Numerical results

5.1 The 2D bar: experiment for long time imbibition phase

We solve the imbibition problem in dimension $d = 2$ setting the following data: the strip Ω has a base of length $L = 0.15$ cm and height equal to $H = 5.85$ cm. Absorption of salts has been observed up to time $T \approx 1.6 \cdot 10^6$ s (almost 4444 hours). The time interval $[0, T]$ has been discretized with step $\Delta t = 3.2$ s, for a number of $5 \cdot 10^6$ temporal samplings. The plots displayed in Figure 5 show the behavior of the quantities θ_l, c_i, c_s and n at the final time instant T at the interior points with $x_1 = 0$

in Ω , so the central vertical axis. Approximations have been obtained by performing the numerical method described in the previous section and discretizing the problem unknowns in space variable with linear finite elements corresponding to a discretization of the boundary of Ω with segments of length $h = h_{x_3} = 0.15$ cm in the vertical direction and $h_{x_1} = 0.075$ cm in the horizontal one, which induces a conforming triangulation of the interior domain.

The finite difference scheme (25) has been performed considering a comparable 1D experiment where the domain Ω is reduced to the interval $x \in [0 \text{ cm}, 5.85 \text{ cm}]$, initial constraints and spatial conditions at the extrema of the interval have been set to replicate the initial and boundary constraints (1) and (3) of the 2D bar. The time step Δt has been set equal to the one of the FEM simulation, as well as $\Delta x = h$, in order to consider the blue lines in Figure 5 as the benchmark results. Let us note that the finite difference discretization is subjected to a CFL condition, leading to a critical choice of the discretization parameters that allows stable 1D results. The plots of the final behavior of the quantities θ_l , c_i , c_s and n obtained with 1D finite differences are shown together with the corresponding FEM results in Figure 5.

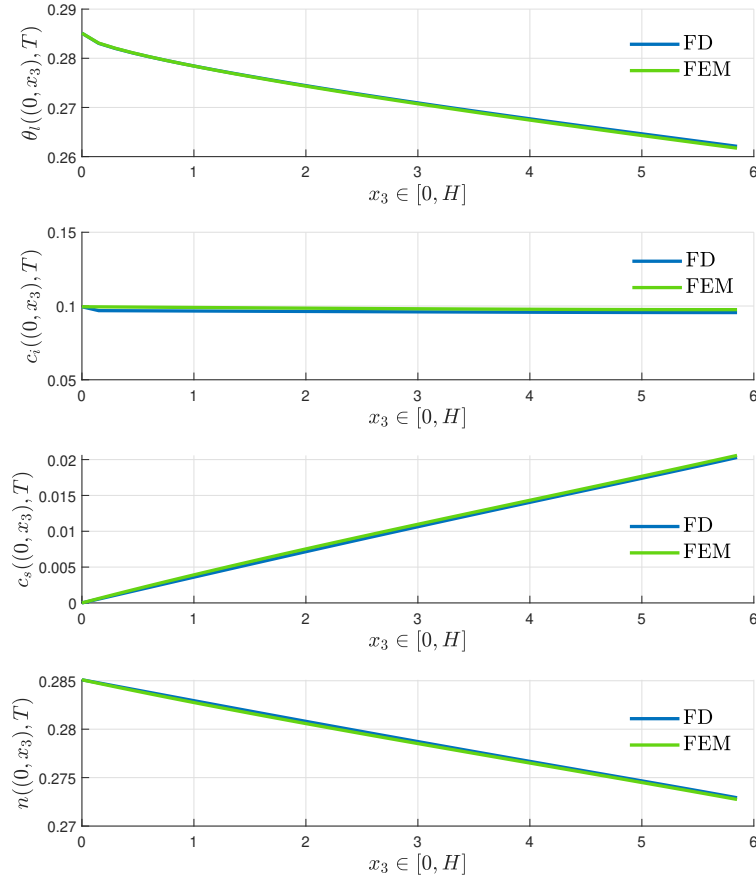


Figure 5: Comparison between 2D finite elements (FEM) and 1D finite difference (FD): the approximation of the quantities θ_l , c_i , c_s and n is shown, for both the employed techniques, at the final instant of water absorption. FEM results have been respectively obtained from the implementation of scheme (17)-(20) and fixing the vertical variable x_3 in the range [0 cm, 5.85 cm] determined by the height of the bar.

5.2 The 2D bar: experiment for imbibition and drying phases

As a second experiment, we solve the imbibition problem by reducing the absorption phase to $T = 4032000$ s (almost 1124 hours) on the same geometry defined for the experiment in subsection 5.1 and for the same initial and boundary conditions. The results for the drying phase have instead been observed up to $\tilde{T} = 2236800$ s (almost 620 hours).

The discretization parameters are the same for both phases: the strip $\Omega = [-0.15 \text{ cm}, 0.15 \text{ cm}] \times [0, 5.85 \text{ cm}]$ has been discretized at the boundary with segments of length $h = h_{x_3} = 0.15 \text{ cm}$ in the vertical direction and $h_{x_1} = 0.075 \text{ cm}$ (inducing a conforming interior triangulation). The time intervals of both phases have been discretized with step $\Delta t = 3.2$ s.

The colormaps displayed in Figure 6 show the behavior of the quantities θ_l, c_i, c_s and n at the final time instant T of the imbibition simulation on the whole rectangular domain Ω . It is evident that the considered absorption time (almost 46 days) is sufficient to completely moisten the bar (values for θ_l are far from the threshold $\bar{\theta}_l$). The other quantities, related to the crystallization phenomena, are characterized by a slower evolution; nevertheless, if we look at the top of the bar, deposit of salt crystals altered the porosity with a decrease of the 1.6% with respect to the baseline n_0 .

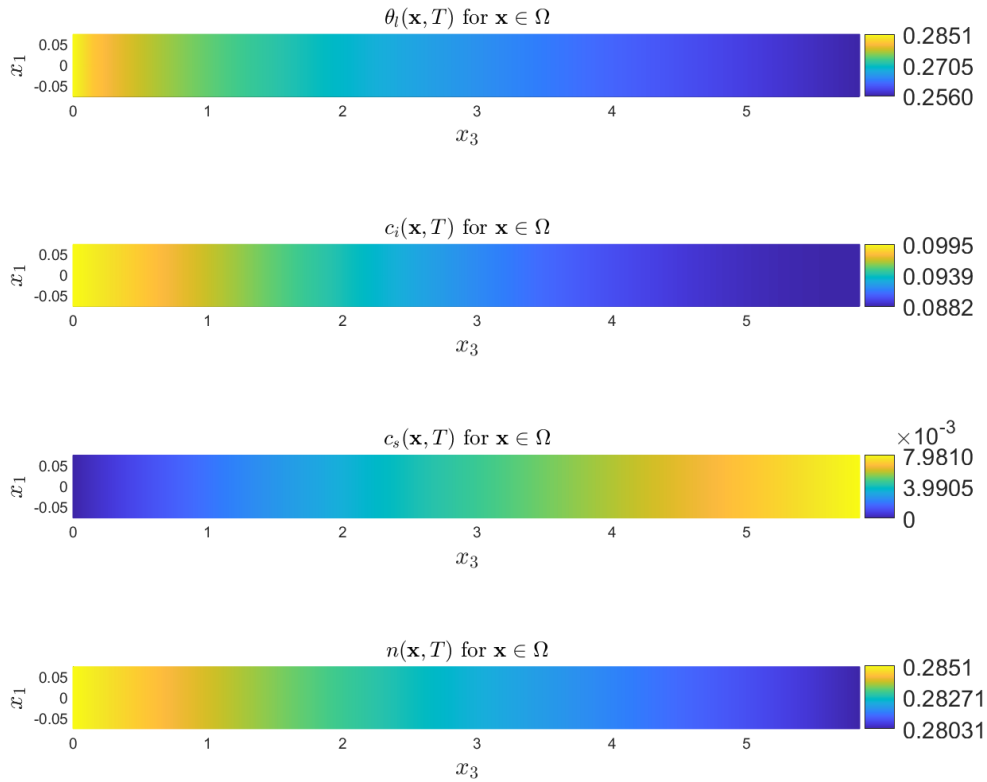


Figure 6: **Water absorption phase.** FEM approximation, at the final instant $T = 4032000$ s, of the fields θ_l, c_i, c_s and n , all displayed on the whole domain $\Omega = [-0.075, 0.075] \times [0, 5.85]$.

The colormaps shown in Figure 7 illustrate the level of the quantities θ_l, c_i, c_s and n at the final time instant \tilde{T} of the drying simulation, again on the whole domain Ω . Constraints for θ_l in (7) in particular induce a reduction of the water volume from the top and the bottom sides of the 2D bar. The free ions concentration c_i at the end of the drying are almost null because of the absence of water supply, while

c_s and n are characterized by a maximum magnitude in Ω of the same order reached at the end of the previous phase of the experiment. As expected, in fact, drying procedure has not significantly changed the quantity of salts already deposited in Ω and, therefore, the porosity of the material itself.

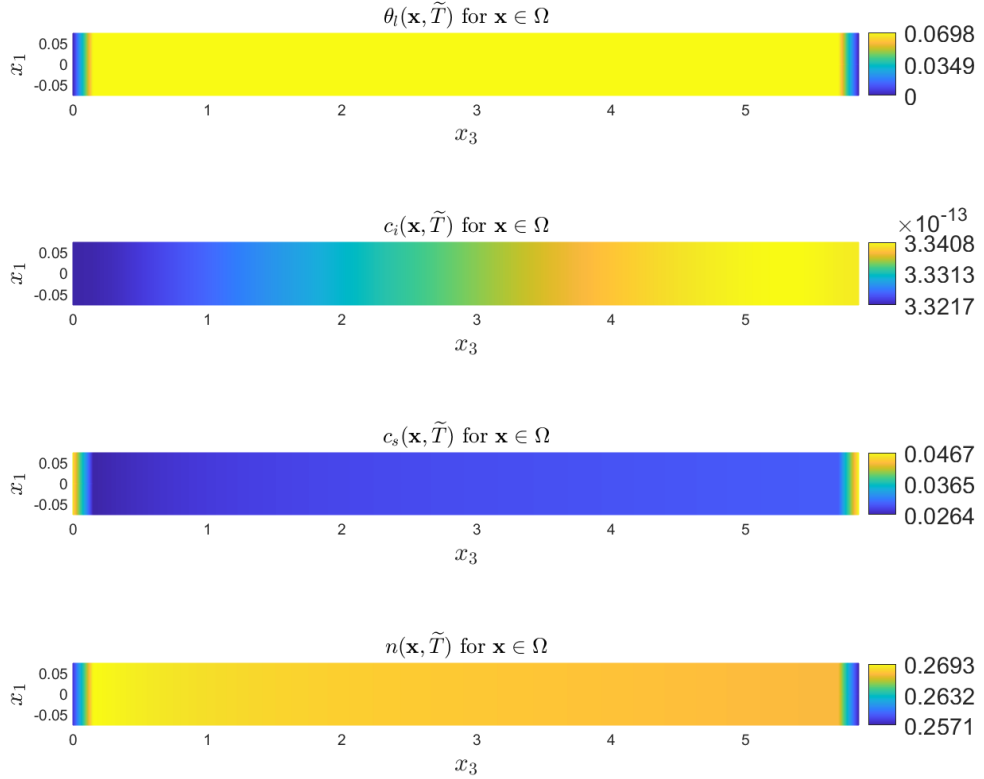


Figure 7: **Drying phase.** FEM approximation, at the final instant $\tilde{T} = 2236800$ s, of the fields θ_l , c_i , c_s and n , all displayed on the whole domain $\Omega = [-0.075, 0.075] \times [0, 5.85]$.

5.3 The 3D bar: a realistic experiment of water absorption and drying

The last experiments consider a realistic geometry in dimension $d = 3$. We considered both the absorption phenomenon, observed up to time $T = 96000$ s, and the drying phase, up to time $\tilde{T} = 32000$ s, for a prism Ω with base edges of length $L = 0.3$ cm and height $H = 0.75$ cm. The chosen temporal step is $\Delta t = 3.2$ s for both the absorption and the drying interval, leading to a total of $3 \cdot 10^4$ and 10^4 instants to study the two phases, respectively. The discretization approach introduced in Section (4) has been performed approximating the problem unknowns in spatial variable in a finite elements perspective induced by a uniform discretization of the boundary edges with segments of length $h = 1.875 \cdot 10^{-2}$ cm. Related uniform triangulation of the external surface and consequent interior discretization with tetrahedral patches lead to an amount of 47396 piecewise linear basis functions for the spatial approximation of the unknowns θ_l , c_i , c_s and n .

Figures (8) and (9) in particular collects approximation results, for the absorption phase, related to θ_l and c_s . Snapshots of their temporal evolution on the surface of the prismatic domain Ω are displayed for different time instants of simulation. It is observable by the 3D plots that growth of θ_l in time, namely the fraction of the absorbed water volume, is faster than the deposit of crystal salts through

the porous matrix, as visible by the fact that the color of the top extreme for the colorbar in figure (8) is reached almost starting from 1280 s , while, at the same instant, the diffusion front of c_s hasn't reached half of the 3D bar yet.

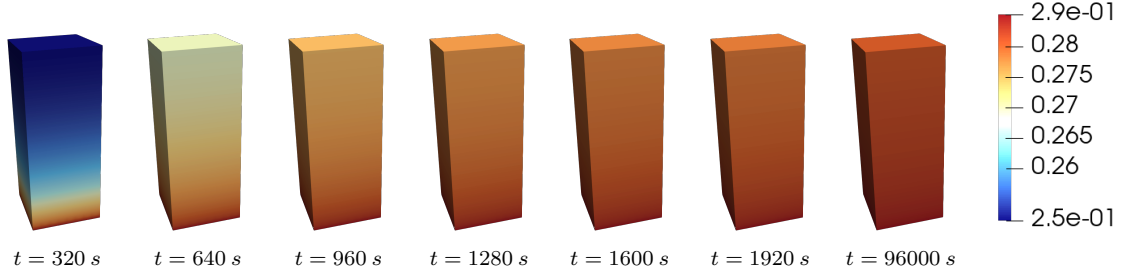


Figure 8: **Absorption phase:** Approximation by spatial finite elements of water density θ_l computed on the 3D domain Ω at different time instants.

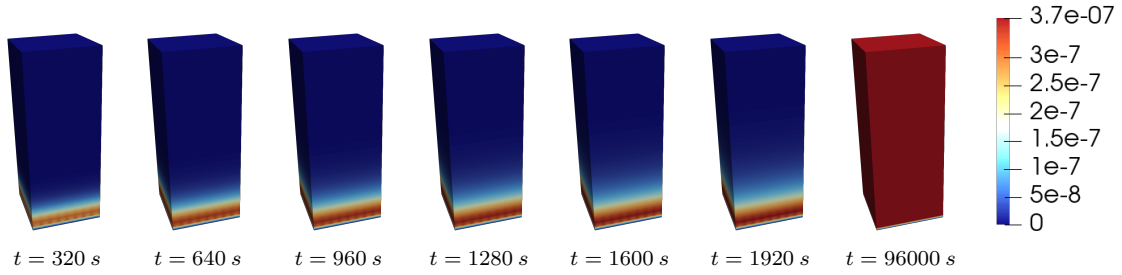


Figure 9: **Absorption phase:** approximation by spatial finite elements of crystals concentration c_s computed on the 3D domain Ω at different time instants.

Snapshots related to the variation during the drying phase, again for θ_l and c_s , are collected in Figures (10) and (11). Boundary conditions (7) force a decrease of the water volume in Ω from the bottom and the top basis, allowing in time a rapid drying of the entire 3D prism, as displayed in Figure 10. Similarly to what was observed for the absorption dynamics, the variation of θ_l is more significant than the other variables. In fact, the frames in Figure (11) show, as expected, that the drying procedure does not alter significantly in time the deposit of crystals obtained at the end of the absorption phase. To quantify the global alteration of porosity at the end of the two phases we chose to employ the metrics for n already introduced in (14), in order to compute the percentage variation of $\mathcal{N}(\gamma, K_s, K_w)$ at the end of the drying phase with respect to its value at beginning of the simulation. In this case, the definition in (14) is trivially extended for the 3D geometry considering a volume integral. We observe that $\mathcal{N} = n_0$ at $t = 0$ because of the initial conditions for n in (1). In the end, the variation with respect to n_0 is small, approximately about 0.00001%. This is justified by the short absorption time, which almost corresponds to one day of water supply. We certainly expect to observe a higher alteration of porosity for a longer experiment.

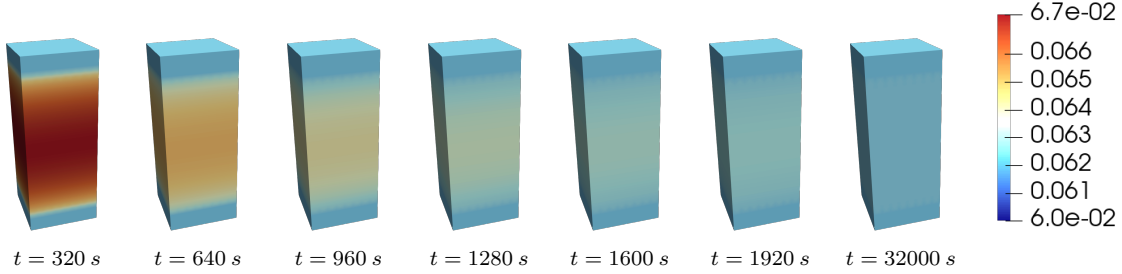


Figure 10: **Drying phase:** approximation by spatial finite elements of water density θ_l computed on the 3D domain Ω at different time instants.

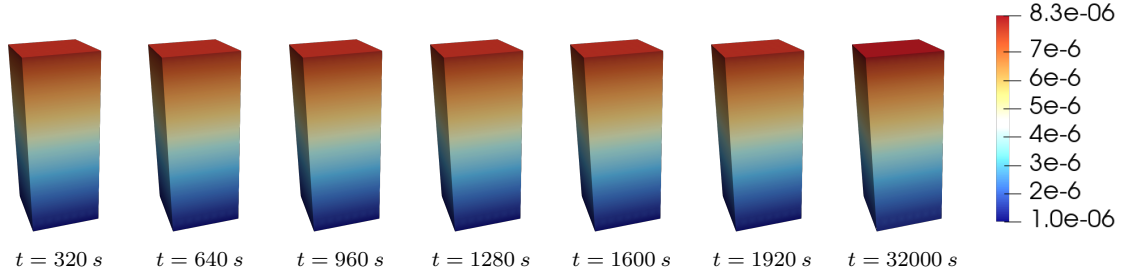


Figure 11: **Drying phase:** approximation by spatial finite elements of crystals concentration c_s computed on the 3D domain Ω at different time instants.

5.4 Experimental convergence analysis

The final numerical subsection is devoted to the experimental convergence analysis of the numerical method proposed in Section 4. The convergence orders are expected to be $O(\Delta t)$ in time and, using linear finite elements and L^2 norm, $O(h^2)$ in space, this latter for all the unknowns except for the field θ_l , since the related nonlinear PDE can downgrade the quadratic decay of the error (see e.g. [33] where, for a nonlinear parabolic PDE, the expected order of convergence in space is proved to be $O(h^2 \log^2(2 + \frac{1}{h}))$).

To do that, we solved system (8)-(11), subjected to the absorption conditions (1)-(3), in the 1D setting. The problem has been numerically solved for various levels of space and time discretization, with accuracy tested introducing the following error, in $L^2(\Omega)$ norm at the final instant of simulation,

$$\mathcal{E}(v) = \left(\int_0^H (v(x, T) - v^{\text{ref}}(x, T))^2 dx \right)^{1/2}, \quad (22)$$

between the unknowns $v = \theta_l, c_i, c_s$ and n and corresponding reference solutions, in this case numerically computed for a sufficiently small values of the refinement parameters.

At first, to recover the convergence order in time, we fix Ω of length $H = 0.6$ cm and the final time of analysis as $T = 2.56 \cdot 10^5$ s, we consider a fixed space refinement of Ω with $h = 3.75 \cdot 10^{-2}$ cm (16 space elements) and we implement the implicit time recursion (17)-(20) for $\Delta t = 16, 8, 4, 2$ s. In Figure 12, the errors $\mathcal{E}(\theta_l)$, $\mathcal{E}(c_i)$ and $\mathcal{E}(c_s)$ are displayed in *log* scale for each considered time step size, using as reference solutions θ_l^{ref} , c_i^{ref} , c_s^{ref} and n^{ref} those obtained using $\Delta t = 0.5$ s. We experimentally deduced a $\mathcal{O}(\Delta t)$ convergence order, as expected by the first order approximation employed in (16).

A second test has been run to recover the convergence order in space. Here, we consider $H = 0.15$ cm and

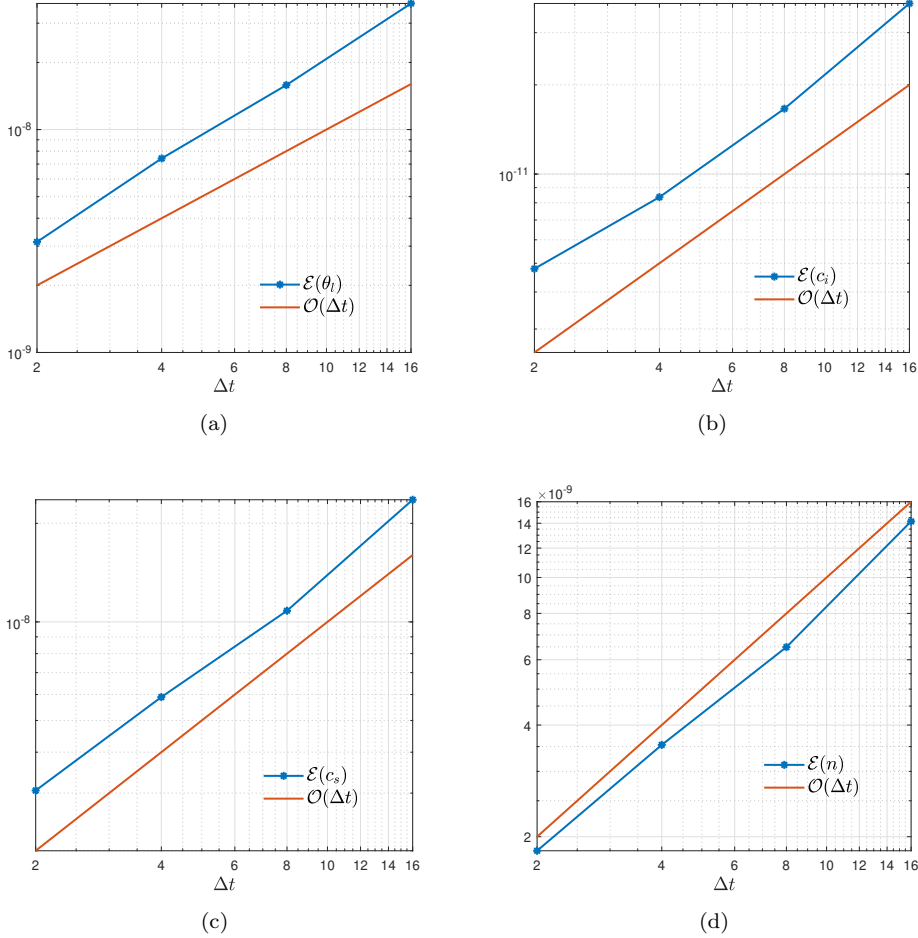


Figure 12: Decay of errors $\mathcal{E}(\theta_l)$ (a), $\mathcal{E}(c_i)$ (b), $\mathcal{E}(c_s)$ (c) and $\mathcal{E}(n)$ (d) considering a fixed space step h and decreasing values of the time step Δt . Together with the errors, the line $\mathcal{O}(\Delta t)$ is represented.

$T = 12$ s. The time step has been kept fixed at $\Delta t = 1e-5$, a value sufficiently small to not let the analysis be influenced by the time approximation error. The unknowns θ_l , c_i , c_s and n have been approximated, in virtue of the implicit time recursion (17)-(20), for an initial uniform spatial discretization of Ω with $h = 0.075$ cm (namely two elements). The procedure has then been repeated halving the space step at each iteration, leading to the plots of $\mathcal{E}(\theta_l)$, $\mathcal{E}(c_i)$, $\mathcal{E}(c_s)$ and $\mathcal{E}(n)$ reported, with respect to the space discretization parameter h , in Figure 13. A quadratic decay is experimentally observed for $\mathcal{E}(c_i)$, $\mathcal{E}(c_s)$ and $\mathcal{E}(n)$, justified by the finite element approximation with linear basis functions of the unknowns c_s , n and c_i in equations (9), (10) and (11). For what concerns instead the error $\mathcal{E}(\theta_l)$ in Figure 13(a), in spite of the same approximation of θ_l field using linear finite elements, its slower convergence is attributable to the non linear behavior of equation (8), influencing, as commented at the beginning of this section, the convergence order in space variable for θ_l .

Remark 3. *From the conducted experimental analysis, we can conjecture that the convergence rate of the FEM approach is superior to the one of the FD scheme recalled in Appendix B.*

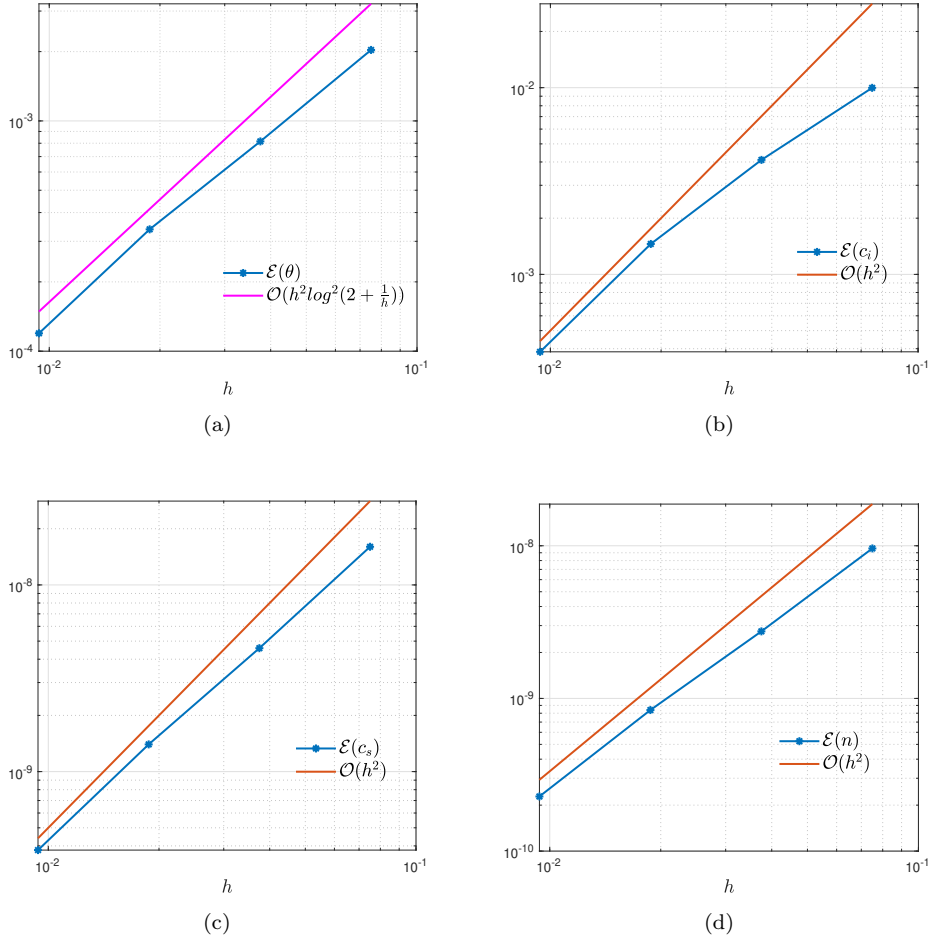


Figure 13: Decay of errors $\mathcal{E}(\theta_l)$ (a), $\mathcal{E}(c_i)$ (b), $\mathcal{E}(c_s)$ (c) and $\mathcal{E}(n)$ (d) considering a fixed time step Δt and decreasing values of the space step h . Together with the errors, the line $\mathcal{O}(h^2)$ is represented in (b), (c), (d), while in (a) a line with slower decay, based on findings in [33], is shown.

6 Conclusions

In this article an extension of the 1D framework in [5] is proposed by using a finite-element space discretization with an implicit-explicit in time approximation. A sensitivity analysis on model parameters calibrated in [5] is performed. Moreover, a numerical study for assessing the experimental order of convergence of FEM VS FD method is carried out, see also the Appendix for more details on FD scheme. The achievements of the present work can be summarized as follows:

- a FEM 3D algorithm is developed for the numerical simulation of salt crystallization in porous materials;
- the numerical convergence rate of FEM is conjectured to be higher than FD one for this problem;
- the robustness of the model with respect to parameters exerting the strongest influence on the crystallization dynamics (γ, K_s, K_w) is assessed;
- the numerical results obtained with FEM algorithm are displayed to show the crystallization process on a brick bar in different experimental settings.

In the future, we will extend the current model to take into account the mechanical damage occurring after a sequence of crystallization cycles, eventually causing important mass decrease of the porous matrix. Moreover, we aim at including the FEM based algorithm on the Stoneverse platform [24].

Acknowledgments

The authors are grateful to Roberto Natalini for the constructive discussions on some features of the mathematical model.

This research was supported by PRIN project MATHPROCULT Prot. P20228HZWR. G.B is responsible of CNR-IAC unit involved in MATHPROCULT project, CUP B53D23015940001. F.F. is responsible of University of Parma unit involved in MATHPROCULT project, CUP D53D23018820001. M.P. is supported by the Project PE0000020 CHANGES - CUP B53C22003890006, PNRR Mission 4 Component 2 Investment 1.3, Funded by the European Union - NextGenerationEU under the Italian Ministry of University and Research (MUR). A.A., G. B., G. D. C., C. G. and M. P. are members of the Gruppo Nazionale Calcolo Scientifico - Istituto Nazionale di Alta Matematica (GNCS-INDAM). M.P. is member of the *Research ITalian network on Approximation* (RITA) and of the SIMAI Group *Numerical and Analytical Approximation of Data and Functions with Applications* (ANA&A).

A Calibration of the top-boundary exchange coefficient

To ensure consistency with the 1D reference model of [5], the exchange coefficient K_w in the Robin boundary condition (3) is calibrated so that the resulting dynamics of moisture and salt match those obtained with the implicit nonlinear boundary condition (NLBC) used in the reference study.

Simulations in 1D are performed using the finite-difference scheme described in (25). For each choice of K_w , the solution is compared with the reference NLBC solution in terms of global quantities, and the relative errors are defined as

$$e_\theta(t) = \frac{\left| \int_0^H \theta(x, t) dx - \int_0^H \theta^{\text{ref}}(x, t) dx \right|}{\int_0^H \theta(x, t) dx}, \quad e_s(t) = \frac{\left| \int_0^H c_s(x, t) dx - \int_0^H c_s^{\text{ref}}(x, t) dx \right|}{\int_0^H c_s(x, t) dx}, \quad (23)$$

where the superscript *ref* denotes the NLBC solution and the subscript for the function $\theta(x, t)$ has been omitted. Furthermore, the time-averaged discrepancy in total water content is defined as

$$M_\theta = \frac{1}{T} \int_0^T e_\theta(t) dt.$$

Here, the integral terms are evaluated using the Second Gregory quadrature rule (see, e.g., [23, 25]). Figure 14 shows that M_θ exhibits a well-defined minimum for $K_w^* = 1.5 \cdot 10^{-2}$. With this choice, the Robin-based simulation closely reproduces the global dynamics of the reference NLBC throughout the imbibition–drying process, both in terms of moisture content and salt crystallization (see Figure 15 for the time evolution of the relative errors). This calibrated value is therefore adopted throughout this work.

B The finite difference scheme

In this appendix, we provide a numerical method based on FD approximations for the simulation of system (8)–(11). The one-dimensional FD framework presented here is adopted to perform sensitivity analysis and investigate boundary conditions in a computationally efficient setting. In view of its use within inverse problems and calibration procedures, which require repeated long-time simulations, we

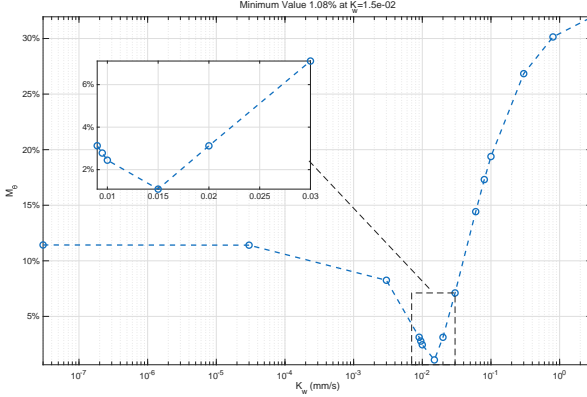


Figure 14: Time-averaged relative error in the total water content for different values of the exchange coefficient K_w .

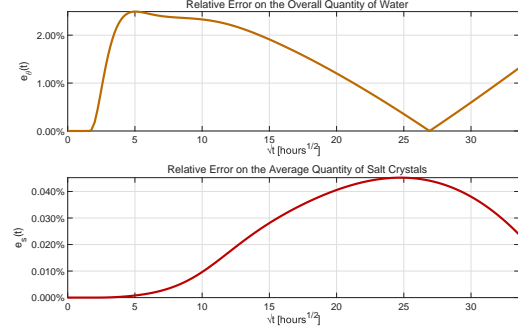


Figure 15: Time evolution of the relative errors for the total water content and salt, comparing the calibrated Robin-based simulation with the reference NLBC solution ($K_w^* = 1.5 \cdot 10^{-2}$).

resort to an explicit, computationally non-demanding, and easily implementable scheme. This setting allows us to assess the robustness of the 1D model (see Section 3) and to consistently retain, in the multi-dimensional extension, the parameters calibrated on experimental data in [5]. Let Δt and Δx denote positive time and space step sizes, respectively. On the space-time domain $[0, H] \times [0, T]$, consider uniform meshes $t_k = k\Delta t$, for $k = 0, \dots, N_t$ and $x_j = j\Delta x$, for $j = 0, \dots, N_x$, with N_t and N_x positive integers such that $T = N_t\Delta t$ and $H = N_x\Delta x$. From now on, for the sake of brevity, we omit the subscript notation for the function $\theta(x, t)$, define the velocity as follows

$$V(\theta(x, t), n(x, t)) = \left(\frac{n(x, t)}{n_0} \right)^2 \frac{\partial B}{\partial z} \left(\frac{\theta(x, t)}{n(x, t)} \right),$$

and denote the numerical approximations by

$$\begin{aligned} \theta_j^k &\approx \theta(x_j, t_k), & c_{s,j}^k &\approx c_s(x_j, t_k), & n_j^k &\approx n(x_j, t_k), & c_{i,j}^k &\approx c_i(x_j, t_k), \\ V_j^k &\approx V(\theta(x_j, t_k), n(x_j, t_k)), & B_j^k &\approx B \left(\frac{\theta(x_j, t_k)}{n(x_j, t_k)} \right) & & & j &= 0, \dots, N_x, \\ & & & & & & k &= 0, \dots, N_t. \end{aligned}$$

We discretize equation (8) by combining a forward FD discretization of the time derivative with the spatial derivative approximation

$$\frac{\partial}{\partial z} \left(r(x_j, t_k) \frac{\partial}{\partial z} w(x_j, t_k) \right) \approx \Delta_j(r^k, w^k) := \frac{(r_j^k + r_{j+1}^k)(w_{j+1}^k - w_j^k) - (r_{j-1}^k + r_j^k)(w_j^k - w_{j-1}^k)}{2\Delta x^2}, \quad (24)$$

for which we refer to [3, 5]. Therefore, we set, for each $j = 1, \dots, N_x - 1$ and $k = 0, \dots, N_t - 1$,

$$\theta_j^{k+1} = \theta_j^k + \Delta t \Delta_j((n^k/n_0)^2, B^k).$$

As for the growth of crystals and the porosity variation, a straightforward FD discretization of (9) and (10) yields

$$\frac{c_{s,j}^{k+1} - c_{s,j}^k}{\Delta t} = K_s c_{i,j}^k (n_j^k - \theta_j^k)^2 + \bar{K} (c_{i,j}^k - \bar{c})_+ \theta_j^k \quad \text{and} \quad n_j^{k+1} = n_0 - \gamma c_{s,j}^{k+1}, \quad \text{for } \begin{cases} j = 0, \dots, N_x, \\ k = 0, \dots, N_t - 1. \end{cases}$$

Finally, recalling (24), equation (11) is discretized, leading to the following numerical scheme

$$\begin{cases} \theta_j^{k+1} = \theta_j^k + \Delta t \Delta_j((n^k/n_0)^2, B^k), & j = 1, \dots, N_x - 1, \\ c_{s,j}^{k+1} = c_{s,j}^k + \Delta t \left[K_s c_{i,j}^k (n_j^k - \theta_j^k)^2 + \bar{K}(c_{i,j}^k - \bar{c})_+ \theta_j^k \right], & j = 0, \dots, N_x, \\ n_j^{k+1} = n_0 - \gamma c_{s,j}^{k+1}, & j = 0, \dots, N_x, \\ c_{i,j}^{k+1} = \frac{1}{\theta_j^{k+1}} \left\{ \theta_j^k c_{i,j}^k + \frac{\Delta t}{2\Delta x} \left(|V_{j+1}^k| c_{i,j+1}^k - 2|V_j^k| c_{i,j}^k + |V_{j-1}^k| c_{i,j-1}^k \right) + \Delta t \Delta_j(D\theta^k, c_i^k) \right. \\ \left. + \frac{\Delta t}{2\Delta x} (V_{j+1}^k c_{i,j+1}^k - V_{j-1}^k c_{i,j-1}^k) - \Delta t \left[K_s c_{i,j}^k (n_j^k - \theta_j^k)^2 + \bar{K}(c_{i,j}^k - \bar{c})_+ \theta_j^k \right] \right\}, & j = 1, \dots, N_x - 1, \end{cases} \quad (25)$$

where, for $k = 0, \dots, N_t - 1$,

$$V_0^k = 0, \quad V_j^k = \left(B \left(\frac{\theta_{j+1}^k}{n_{j+1}^k} \right) - B \left(\frac{\theta_{j-1}^k}{n_{j-1}^k} \right) \right) \frac{(n_j^k/n_0)^2}{2\Delta x}, \quad j = 1, \dots, N_x - 1. \quad (26)$$

We remark that the additional term

$$\frac{|V_{j+1}^k| c_{i,j+1}^k - 2|V_j^k| c_{i,j}^k + |V_{j-1}^k| c_{i,j-1}^k}{2\Delta x}, \quad (27)$$

appearing in the discrete sodium sulfate concentration equation provides an upwind-type stabilization of the nonlinear convective flux $\text{div}(c_i(x, t)V(\theta(x, t), n(x, t)))$. This contribution does not represent a finite-difference approximation of a differential operator in the continuous model (11). Rather, it arises from the stabilization of the convective term and corresponds, at the level of the modified equation, to a numerical viscosity with coefficient proportional to $|V| \Delta x$, which vanishes as the spatial mesh is refined. The inclusion of this term improves the robustness of the explicit scheme in convection-dominated regimes and prevents non-physical oscillations of the concentration field. Similar stabilization mechanisms are standard in the numerical approximation of transport problems (see, e.g., [19, 21]).

The initial conditions (1) and the boundary conditions (2)–(3) are discretized as follows

$$\theta_j^0 = \begin{cases} n_0 & \text{if } j = 0, \\ \bar{\theta}_l & \text{if } j > 0, \end{cases} \quad c_{s,j}^0 = 0, \quad c_{i,j}^0 = \begin{cases} \bar{c}_i & \text{if } j = 0, \\ 0 & \text{if } j > 0, \end{cases} \quad n_j^0 = n_0, \quad j = 0, \dots, N_x, \quad (28)$$

$$\theta_0^k = n_0^k, \quad \theta_N^k = \frac{4\theta_{N_x-1}^k - \theta_{N_x-2}^k + 2\Delta x K_w \bar{\theta}_l}{3 + 2\Delta x K_w}, \quad c_{i,0}^k = \bar{c}_i, \quad c_{i,N_x}^k = \frac{4}{3} c_{i,N_x-1}^k - \frac{1}{3} c_{i,N_x-2}^k, \quad (29)$$

for $k = 1, \dots, N_t$, obtained from a second order, backward in space finite difference approximation of the derivative operator (we refer to [22, 26] for a comprehensive overview on FD schemes). Analogous discretizations are employed for the drying conditions (5)–(7).

Under standard smoothness assumptions, the finite difference scheme (25) is expected to be convergent with at least first-order accuracy in both time and space. Numerical investigations, omitted here for the sake of conciseness, support this claim.

References

[1] M. Alnæs, J. Blechta, J. Hake, A. Johansson, B. Kehlet, A. Logg, C. Richardson, J. Ring, M.E. Rognes, and G.N. Wells. The FEniCS Project Version 1.5. *Archive of Numerical Software*, 3(100), 2015. [doi:10.11588/ans.2015.100.20553](https://doi.org/10.11588/ans.2015.100.20553).

[2] G G Amoroso and V Fasina. *Stone decay and conservation; Atmospheric pollution, cleaning; and consolidation*. Elsevier Science Pub., New York, NY, 01 1983. URL: <https://www.osti.gov/biblio/5767685>.

[3] D. Aregba-Driollet, F. Diele, and R. Natalini. A Mathematical Model for the Sulphur Dioxide Aggression to Calcium Carbonate Stones: Numerical Approximation and Asymptotic Analysis. *SIAM Journal on Applied Mathematics*, 64(5):1636–1667, 2004. [doi:10.1137/S003613990342829X](https://doi.org/10.1137/S003613990342829X).

[4] E. Bonetti, C. Cavaterra, F. Freddi, M. Grasselli, and R. Natalini. A nonlinear model for marble sulphation including surface rugosity and mechanical damage. *Nonlinear Analysis: Real World Applications*, 73:103886, 2023. [doi:10.1016/j.nonrwa.2023.103886](https://doi.org/10.1016/j.nonrwa.2023.103886).

[5] M.P. Bracciale, G. Bretti, A. Broggi, M. Ceseri, A. Marrocchi, R. Natalini, and C. Russo. Mathematical modelling of experimental data for crystallization inhibitors. *Applied Mathematical Modelling*, 48:21–38, 2017. [doi:10.1016/j.apm.2016.11.026](https://doi.org/10.1016/j.apm.2016.11.026).

[6] E. C. Braun, G. Bretti, M. Di Fazio, L. Medeghini, and M. Pezzella. Data-Informed Mathematical Characterization of Absorption Properties in Artificial and Natural Porous Materials. *arXiv*, 2025. [doi:10.48550/arXiv.2506.07656](https://doi.org/10.48550/arXiv.2506.07656).

[7] G. Bretti and C. M. Belfiore. Mathematical modelling of water absorption properties for historical lime-based mortars. *GEM - International Journal on Geomathematics*, 16(1):18, Sep 2025. [doi:10.1007/s13137-025-00275-2](https://doi.org/10.1007/s13137-025-00275-2).

[8] G. Bretti, M. Ceseri, R. Natalini, M. C. Ciacchella, M. L. Santarelli, and G. Tiracorrendo. A forecasting model for the porosity variation during the carbonation process. *Int J Geomath*, 13(13), 2022. [doi:10.1007/s13137-022-00204-7](https://doi.org/10.1007/s13137-022-00204-7).

[9] G. Bretti, B. De Filippo, R. Natalini, S. Goidanich, M. Roveri, and L. Toniolo. Modelling the effects of protective treatments in porous materials. In Elena Bonetti, Cecilia Cavaterra, Roberto Natalini, and Margherita Solci, editors, *Mathematical Modeling in Cultural Heritage*, pages 73–83. Springer International Publishing, 2021. [doi:10.1007/978-3-030-58077-3_5](https://doi.org/10.1007/978-3-030-58077-3_5).

[10] G. Bretti and R. Natalini. Forecasting damage and consolidation: Mathematical models of reacting flows in porous media. In Gabriella Bretti, Cecilia Cavaterra, Margherita Solci, and Michela Spagnuolo, editors, *Mathematical Modeling in Cultural Heritage*, pages 187–207. Springer Nature Singapore, 2023.

[11] M. Ceseri, R. Natalini, and M. Pezzella. An Integro-Differential Model of Cadmium Yellow Photodegradation. *SIAM Journal on Applied Mathematics*, 85(6):2591–2610, 2025. [doi:10.1137/24M1709704](https://doi.org/10.1137/24M1709704).

[12] A.E. Charola and E. Wendler. An overview of the water-porous building materials interactions. *Restoration of Buildings and Monuments*, 21(1):5565, 2015. [doi:10.1515/rbm-2015-0006](https://doi.org/10.1515/rbm-2015-0006).

[13] F. Clarelli, R. Natalini, C. Nitsch, and M. L. Santarelli. *A Mathematical Model for Consolidation of Building Stones*, volume Volume 82 of *Series on Advances in Mathematics for Applied Sciences*, pages 232–243. WORLD SCIENTIFIC, Sep 2009. [doi:10.1142/9789814280303_0021](https://doi.org/10.1142/9789814280303_0021).

[14] E. Doehe. Salt weathering: a selective review. *Geological Society, London, Special Publications*, 205(1):51–64, 2002. [doi:10.1144/GSL.SP.2002.205.01.05](https://doi.org/10.1144/GSL.SP.2002.205.01.05).

[15] M. El-Khoury, F. Grondin, E. Roziere, Cortas Rachid, and Chehade Hage Fadi. Chemical degradation vs. creep loading vs. hydration processes in cement-based materials immerged

in seawater characterized with a multiscale model. *Mech Time-Depend Mater*, 29(63), 2025. [doi:10.1007/s11043-025-09792-x](https://doi.org/10.1007/s11043-025-09792-x).

[16] F. Freddi and L. Mingazzi. A predictive phase-field approach for cover cracking in corroded concrete elements. *Theoretical and Applied Fracture Mechanics*, 122:103657, 2022. [doi:10.1016/j.tafmec.2022.103657](https://doi.org/10.1016/j.tafmec.2022.103657).

[17] F. Guaraguaglini. A degenerate parabolic model for chemical reactions in porous rocks: existence of solutions. *MEMOCS*, 13(2):167200, 2025. [doi:10.2140/memocs.2025.13.69](https://doi.org/10.2140/memocs.2025.13.69).

[18] F. Guaraguaglini. Existence of solutions to a boundary problem for one dimensional degenerate parabolic models for chemical reactions in porous rocks, 2026.

[19] J.L. Guermond and B. Popov. Invariant Domains and Second-Order Continuous Finite Element Approximation for Scalar Conservation Equations. *SIAM Journal on Numerical Analysis*, 55(6):3120–3146, 2017. [doi:10.1137/16M1106560](https://doi.org/10.1137/16M1106560).

[20] G. D. Hoke and D. L. Turcotte. Weathering and damage. *Journal of Geophysical Research: Solid Earth*, 107(B10):ECV 1–1–ECV 1–6, 2002. [doi:10.1029/2001JB001573](https://doi.org/10.1029/2001JB001573).

[21] Randall J. LeVeque. *Finite Volume Methods for Hyperbolic Problems*. Cambridge University Press, 2002. [doi:10.1017/cbo9780511791253](https://doi.org/10.1017/cbo9780511791253).

[22] R.J. LeVeque. *Finite Difference Methods for Ordinary and Partial Differential Equations*. Society for Industrial and Applied Mathematics, 2007. [doi:10.1137/1.9780898717839](https://doi.org/10.1137/1.9780898717839).

[23] E. Messina, M. Pezzella, and A. Vecchio. A long-time behavior preserving numerical scheme for age-of-infection epidemic models with heterogeneous mixing. *Applied Numerical Mathematics*, 200:344–357, 2024. New Trends in Approximation Methods and Numerical Analysis (FAATNA20>22). [doi:10.1016/j.apnum.2023.04.009](https://doi.org/10.1016/j.apnum.2023.04.009).

[24] E. Onofri, S. Bizzarro, S. Tassa, M. Czech, and G. Brett. Models and Methods in Cultural Heritage. StoneVerse: the open-science platform for cultural heritage. In *Digital Heritage 2025*, 2025.

[25] Pezzella, M. High order positivity-preserving numerical methods for a non-local photochemical model. *ESAIM: M2AN*, 59(3):1763–1790, 2025. [doi:10.1051/m2an/2025041](https://doi.org/10.1051/m2an/2025041).

[26] A. Quarteroni, R. Sacco, and F. Saleri. *Numerical Mathematics*. Springer New York, 2007. [doi:10.1007/b98885](https://doi.org/10.1007/b98885).

[27] S. Razavi and H. V. Gupta. What do we mean by sensitivity analysis? The need for comprehensive characterization of global sensitivity in Earth and Environmental systems models. *Water Resources Research*, 51(5):3070–3092, 2015. [doi:10.1002/2014WR016527](https://doi.org/10.1002/2014WR016527).

[28] R. Reale, L. Campanella, M. P. Sammartino, G. Visco, G. Brett, M. Ceseri, R. Natalini, and F. Notarnicola. A mathematical, experimental study on iron rings formation in porous stones. *Journal of Cultural Heritage*, 38:158–166, 2019. [doi:10.1016/j.culher.2019.01.012](https://doi.org/10.1016/j.culher.2019.01.012).

[29] S. Siegesmund, J. Menningen, and V. Shushakova. Marble decay: towards a measure of marble degradation based on ultrasonic wave velocities and thermal expansion data. *Environ Earth Sci*, 80(395), 2021. [doi:10.1007/s12665-021-09654-y](https://doi.org/10.1007/s12665-021-09654-y).

[30] M. Steiger, K. Linnow, H. Juling, G. Gürker, A.E. Jarad, S. Brüggerhoff, and D. Kirchner. Hydration of $MgSO_4 \cdot H_2O$ and Generation of Stress in Porous Materials. *Crystal Growth & Design*, 8(1):336–343, 2008. [doi:10.1021/cg060688c](https://doi.org/10.1021/cg060688c).

- [31] Q. Wang, C. Cheng, E. Agathokleous, Y. Liu, X. Li, and X. Sheng. Enhanced diversity and rock-weathering potential of bacterial communities inhabiting potash trachyte surface beneath mosses and lichens A case study in Nanjing, China. *Science of The Total Environment*, 785:147357, 2021. [doi:10.1016/j.scitotenv.2021.147357](https://doi.org/10.1016/j.scitotenv.2021.147357).
- [32] Th. Warscheid and J. Braams. Biodeterioration of stone: a review. *International Biodeterioration & Biodegradation*, 46(4):343–368, 2000. Biodeterioration of Cultural Property 2, Part 2. [doi:10.1016/S0964-8305\(00\)00109-8](https://doi.org/10.1016/S0964-8305(00)00109-8).
- [33] C. Yang. Convergence of a linearized second-order BDF-FEM for nonlinear parabolic interface problems. *Computers and Mathematics with Applications*, 70(3):265–281, 2015. [doi:10.1016/j.camwa.2015.05.006](https://doi.org/10.1016/j.camwa.2015.05.006).
- [34] Y. Zhang, D. M. Pedroso, and L. Li. FDM and FEM solutions to linear dynamics of porous media: stabilised, monolithic and fractional schemes. *International Journal for Numerical Methods in Engineering*, 108(6):614–645, 2016. [doi:10.1002/nme.5231](https://doi.org/10.1002/nme.5231).